ACS OMEGA

http://pubs.acs.org/journal/acsodf

Article

Enhancing the Electrochemical Properties of Ti-Doped $LiMn_2O_4$ Spinel Cathode Materials Using a One-Step Hydrothermal Method

Yaqing Zhang, Hongyan Xie,* Huixin Jin, Xiaohui Li, Qiang Zhang, Yezhu Li, KaiFeng Li, Fenglan Luo, Wenlei Li, and Chenzhe Li

Cite This: *ACS Omega* 2021, 6, 21304−21315

Read Online

ACCESS | Metrics & More | Article Recommendations

ABSTRACT: In this study, $LiMn_{2-x}Ti_xO_4$ cathode materials were synthesized by a simple one-step hydrothermal method, and the effects of Ti doping on the sample structure and electrochemical properties were examined. The results indicated that Ti doping did not affect the spinel structure of $LiMn_2O_4$, and no other hybrid phases were produced. Furthermore, appropriate doping with Ti improved the particle uniformity of the samples. The electrochemical performance results showed that $LiMn_{1.97}Ti_{0.03}O_4$ exhibited much better cycling performance than the undoped sample. The discharge capacity of $LiMn_{1.97}Ti_{0.03}O_4$ reached 136 mAh g^{-1} at 25 °C at 0.2C, and the specific capacity reached 106.2 mAh g^{-1} after 300 cycles, with a capacity retention rate of 78.09%. Additionally, the specific capacity of $LiMn_{1.97}Ti_{0.03}O_4$ was 102.3 mAh g^{-1} after 100 cycles at 55 °C, with a capacity retention rate of 75.44%. The Ti-doped samples thus exhibited an impressive high-rate performance. The discharge capacity of $LiMn_2O_4$ was only 31.3 mAh g^{-1} at 10C, while the discharge-specific capacity of $LiMn_{1.97}Ti_{0.03}O_4$ reached 73.4 mAh g^{-1}. Furthermore, to assess the higher Li^+ diffusion coefficient and lower internal resistance of the Ti-doped samples, cyclic voltammetry and impedance spectra data were obtained. Our results showed that Ti doping enhanced the crystal structure of $LiMn_2O_4$ and improved Li^+ diffusion, resulting in significant improvements in the cycling and rate performance of Ti-doped samples.

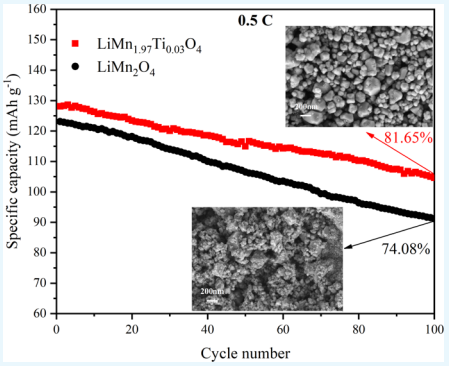

1. INTRODUCTION

Safe and portable lithium-ion batteries are one of the newest rechargeable energy storage devices that are frequently used in everyday life. Characterized by high energy density and high cycle life, lithium-ion batteries have attracted considerable attention.[1−6] Compared to other cathode materials, spinel $LiMn_2O_4$ has the advantages of abundant resources, low cost, safety, nontoxicity, environmental friendliness, and superior performance.[7,8] However, its commercial applications are limited due to issues with rapid capacity decay, which is mainly caused by Mn^{3+} ion Jahn−Teller distortion.[9−13] This distortion occurs when the $LiMn_2O_4$ crystal structure changes from cubic to quadrate rock salt during the final discharging process, blocking the Li^+ ion diffusion channel.[14,15] Additionally, due to the disproportionation of the manganese ions, Mn inevitably dissolves in the electrolyte solution,[16] resulting in a decrease in the active substance and attenuation capacity.

To solve the aforementioned problems, many methods have been studied and utilized. Element doping is an effective method to improve the cycling performance of $LiMn_2O_4$ and includes metal-ion doping (Al^{3+}, Cr^{3+}, Mg^{2+}, Ni^{2+}),[17−21] nonmetal ion doping (Si^{4+}, F^-),[22,23] and ionic codoping.[24−26] Gu et al.[27] studied the electrochemical performance of $LiMn_{2-x}M_xO_4$ (M = Mn, Co, Ni, Fe, Cr, Al; x = 0.05, 0.1, 0.15, and 0.2) and showed that doping of metal ions effectively blocks the crystal phase transition, reducing the microstrain and volume contractions during the cycling process. Furthermore, $LiMn_{2-x}M_xO_4$ exhibited better electrochemical stability and less capacity fading than $LiMn_2O_4$ did. Numerous previous studies[28−30] have also shown that low-priced metal ions can replace Mn compounds and can also enter the 16d octahedral sites, thus improving the average Mn valence state in spinel $LiMn_2O_4$ while reducing the amount of Mn^{3+} ions. This method inhibits Jahn−Teller distortion, stabilizes the structure during the charging and discharging processes, and improves the cycling performance. However, few studies have examined the electrochemical performance of Ti^{4+}-doped $LiMn_2O_4$. Furthermore, because the Ti−O bond has stronger binding energy than Mn−O, it can form a more stable $[Mn_{2-x}Ti_x]O_4$ skeleton and potentially improve the material cycling performance.

Received: March 22, 2021
Accepted: June 10, 2021
Published: August 10, 2021

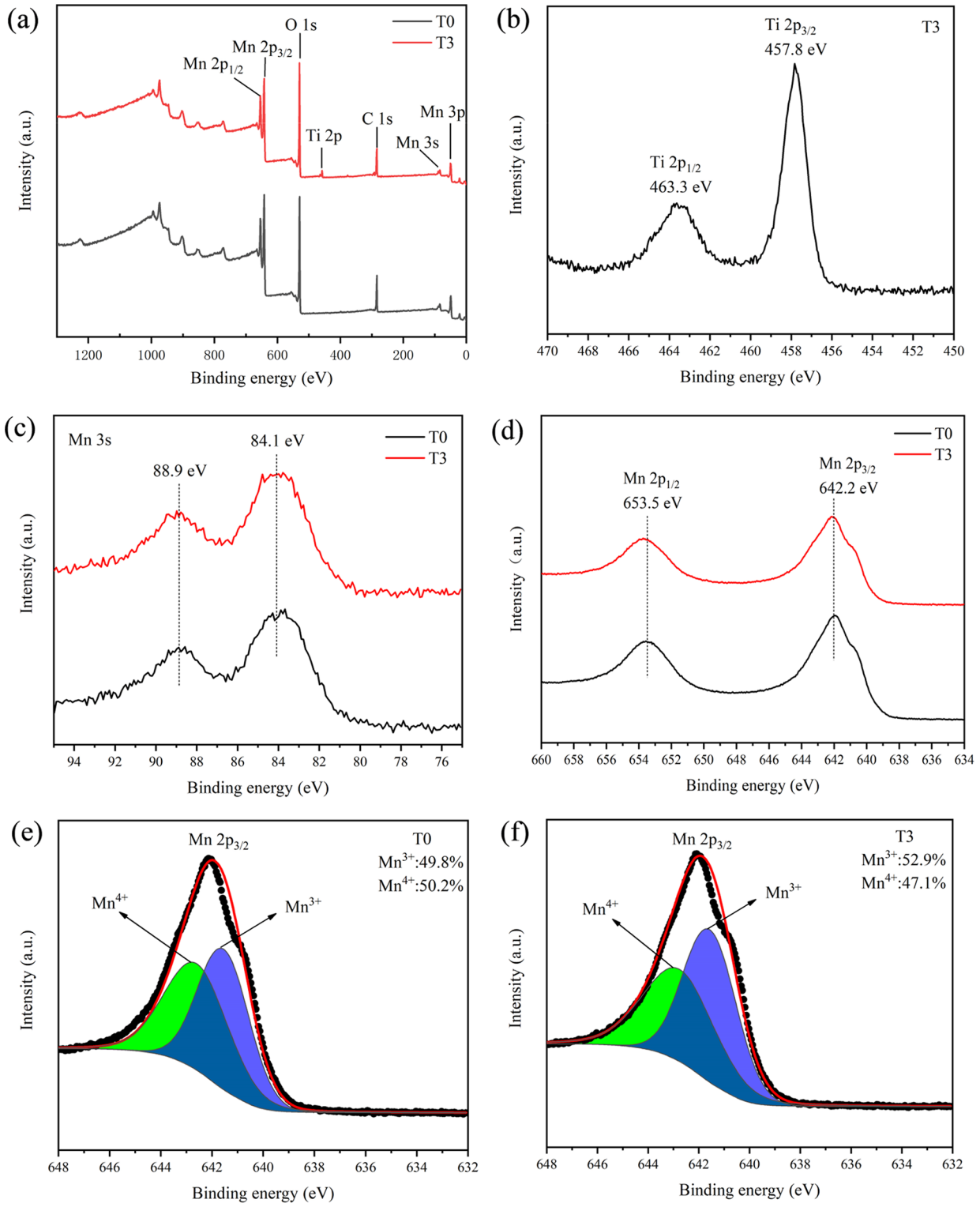

Figure 1. (a) XPS full spectrum of the T0 and T3 samples, (b) Ti 2p peaks of T3, (c) Mn 3s peaks of T0 and T3, (d) Mn 2p peaks of T0 and T3, (e) fitted Mn $2p_{3/2}$ peaks of T0, and (f) fitted Mn $2p_{3/2}$ peaks of T3.

Additionally, choosing a synthetic method significantly impacts the use of spinel $LiMn_2O_4$ in Li-ion batteries, as material performance is closely related to morphology, size, and structure.[31] Various high-capacity and high-cycling performance methods for the preparation of spinel $LiMn_2O_4$ have been proposed, including the Pechini, sol−gel, and hydrothermal methods.[32−36] Tian et al.[37] proposed a rapid synthesis of $LiMn_2O_4$ using a microwave-induced flameless combustion solution method. The heat treatment of lithium nitrate, manganese acetate, tetrahydrate, and nitric acid at 105 °C formed a eutectic solution. Following this, the solution underwent a flameless combustion reaction at temperatures between 300 and 700 °C, and the final synthesized $LiMn_2O_4$ structure was composed of submicron polyhedral crystals. The

https://doi.org/10.1021/acsomega.1c01521
ACS Omega 2021, 6, 21304−21315

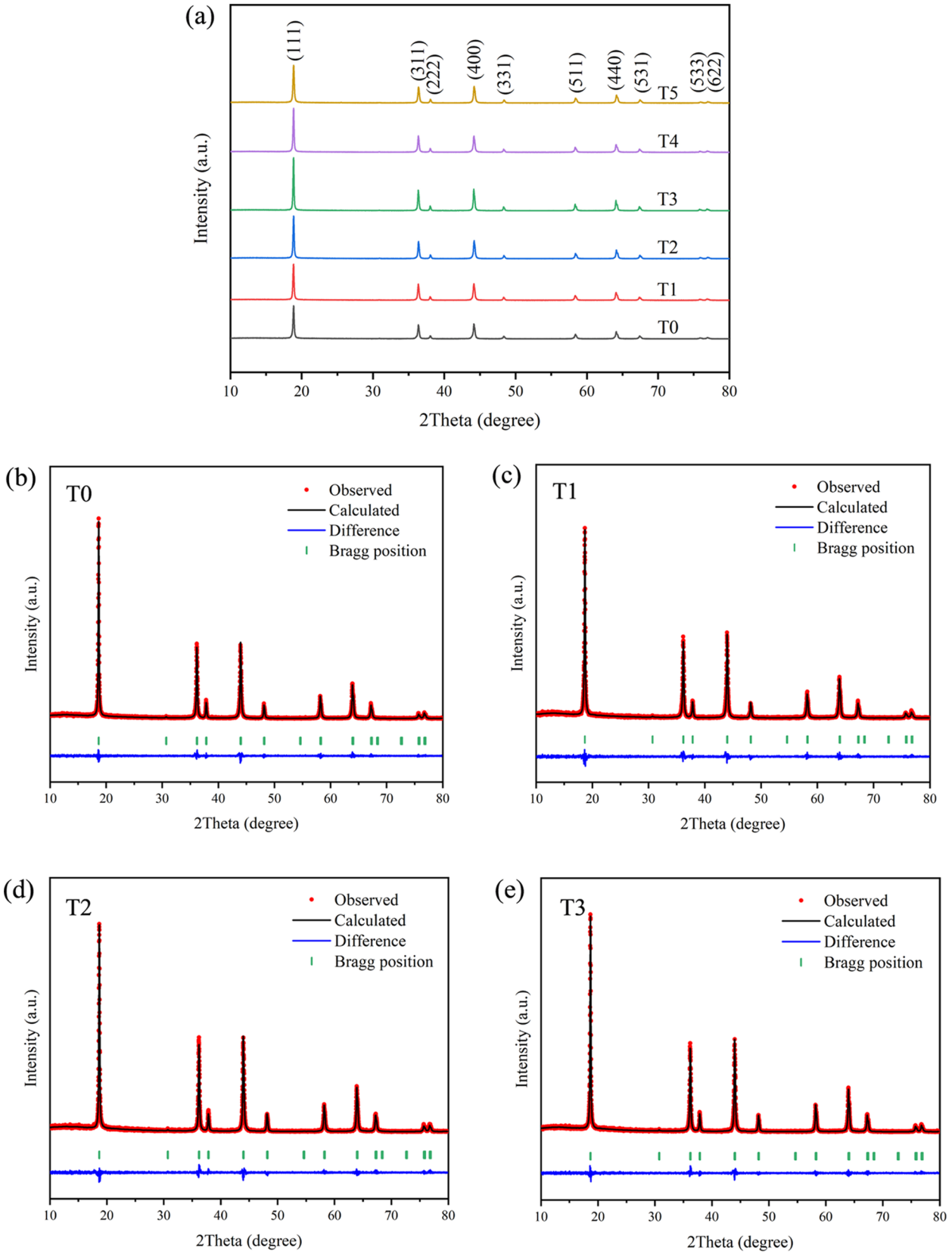

Figure 2. continued

https://doi.org/10.1021/acsomega.1c01521
ACS Omega 2021, 6, 21304−21315

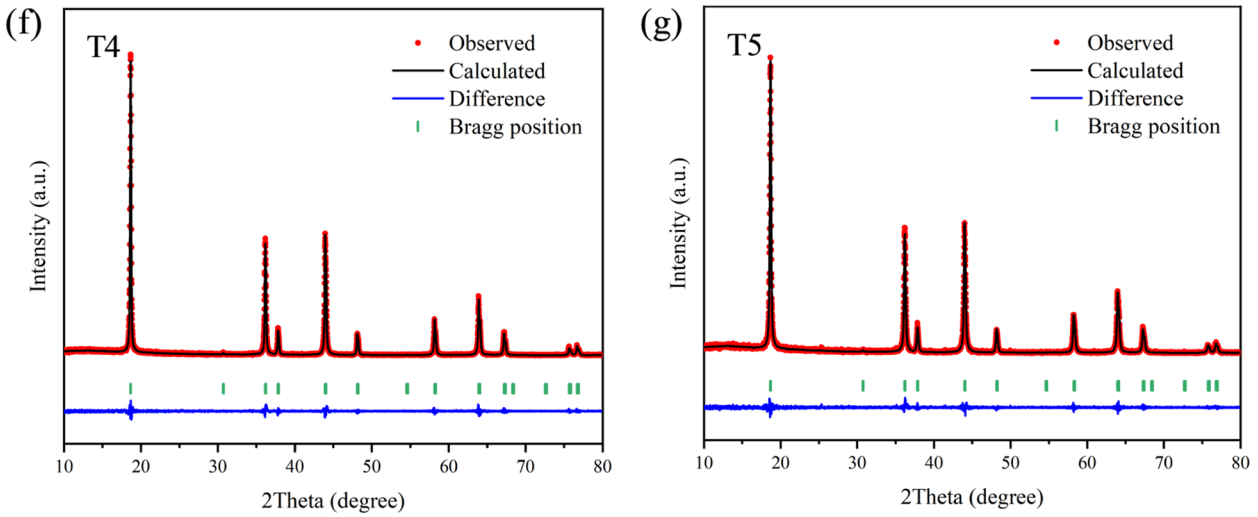

Figure 2. (a) XRD patterns of samples from T0 to T5. Rietveld refinement for the samples of (b) T0, (c) T1, (d) T2, (e) T3, (f) T4, and (g) T5.

Table 1. Atom Occupancy Parameters Obtained from Rietveld Refinement

		occupancy					
atom	site	T0	T1	T2	T3	T4	T5
Li	8a	0.0417	0.0417	0.0417	0.0417	0.0417	0.0417
Mn	16d	0.0832	0.0825	0.0817	0.0805	0.0792	0.0781
Ti1	8a						
Ti2	16d		0.0006	0.0015	0.0028	0.0037	0.0047
O	32e	0.1667	0.1667	0.1667	0.1667	0.1667	0.1667

discharge capacity reached 114.4 mAh g^{-1} at 1C, with a capacity retention of 45.4% after 1000 cycles. Chen et al.[38] synthesized mesoporous spinel $LiMn_2O_4$ with high crystallinity via a soft-templating method that used a two-step heat-treatment process. The results showed that the mesoporous spinel $LiMn_2O_4$ exhibited higher Li^+ diffusion, and the mesoporous structure promoted the rapid transport and intercalation dynamics of Li^+, giving it good cycle capabilities at a high current density. However, most of these studies adopted a complicated two-step synthesis, where the precursor ($MnCO_3$, MnO_2, and Mn_3O_4) was first synthesized using a liquid phase method, followed by high-temperature calcination (700−900°C) for secondary grain growth.

In this work, Ti-doped spinel $LiMn_2O_4$ was prepared using a simple one-step hydrothermal method that was quick, direct, and effective and did not require any preprocessing. Supporting the existing research, we found that doping Ti ions significantly slowed the capacity decay problem of spinel $LiMn_2O_4$ and improved its electrochemical performance.

2. RESULTS AND DISCUSSION

2.1. Structure and Morphology. Figure 1 shows the X-ray photoelectron spectra (XPS) of the T0 and T3 samples. A full-range XPS spectrum is shown in Figure 1a, and the characteristic peaks of C 1s, O 1s, Mn 2p, and Mn 3s are visible in both T0 and T3 samples. Specifically, detection of the Ti 2p peak confirmed the presence of the Ti element in the T3 sample. Figure 1b shows the Ti 2p XPS spectrum, and the Ti 2p was split into two peaks, which were Ti $2p_{3/2}$ (457.8 eV) and Ti $2p_{1/2}$ (463.3 eV). The binding energy between $2p_{3/2}$ and $2p_{1/2}$ differed by 5.5 eV, indicating that the Ti ions were in a tetravalent oxidation state. To confirm the oxidation state of the Mn ions, a Mn 3s spectrum analysis was performed on the sample, as shown in Figure 1c, and the energy intervals of the 3s multiple splitting peaks for Mn^{2+}, Mn^{3+}, and Mn^{4+} were 6.1, 5.5, and 4.5 eV, respectively. The energy split of the samples was 4.8 eV, which was between Mn^{3+} (5.5 eV) and Mn^{4+} (4.5 eV), confirming that the oxidation states of the Mn ions in the T0 and T3 samples were +3 and +4. Figure 1d shows the Mn 2p spectrum, for which the binding energies of Mn $2p_{3/2}$ and Mn $2p_{1/2}$ were 642.1 and 653.8 eV, with a separation of 11.7 eV. As shown in Figure 1e,f, the Mn $2p_{3/2}$ curves fit the two peaks at approximately 642.8 and 641.7 eV, corresponding to Mn^{3+} and Mn^{4+}, respectively.[39] The Mn^{3+}/Mn^{4+} percentage ratios for the T0 and T3 samples were 49.8/50.2 and 52.9/7.1%, respectively, as obtained from the different photoelectron peak area ratios. Thus, the results showed that doping the Ti^{4+} ions increased the Mn^{3+}/Mn^{4+} ratio, indicating that Ti^{4+} replaced the Mn^{4+} sites in the material crystal structure.

Figure 2a shows the X-ray diffraction (XRD) patterns for all of the samples. The samples showed the characteristic cubic spinel structure diffraction peaks with $Fd\bar{3}m$ symmetry and no other impurity phase peaks, indicating that introducing trace amounts of Ti^{4+} did not change the inherent spinel structure. Moreover, the diffraction peak strength of the doped Ti sample was higher than that of the undoped sample, indicating that Ti doping moderately enhanced the crystallinity of the material. Rietveld refinement using the FULLPROF software was also conducted as part of the XRD data analysis, as shown in Figure 2b−g. The results are listed in Tables 1 and 2. The small confidence profile R-factor, R_{wp}, confirmed that the results were credible. Table 1 shows the atom occupancy parameters, indicating that the Ti^{4+} ions that occupied the Mn position as a result of Ti doping, forming a stable $[Mn_{2-x}Ti_x]O_4$ skeleton. Table 2 shows the lattice parameters and cell volumes of the samples. Table 2 shows the sample lattice parameters, as well as the cell volumes,

https://doi.org/10.1021/acsomega.1c01521
ACS Omega 2021, 6, 21304−21315

Table 2. Crystallographic Data Obtained from Rietveld Refinement

sample	a (Å)	V (Å^3)	R_{wp} (%)
T0	8.2267	556.775	8.42
T1	8.2301	557.464	8.14
T2	8.2328	558.018	7.75
T3	8.2333	558.107	7.92
T4	8.2343	558.309	9.17
T5	8.2349	558.437	8.85

which increased as the Ti doping amount increased. This likely occurred because Ti^{4+} ions have a larger radius (0.61 Å), replacing the smaller-radius Mn^{4+} ions (0.53 Å). The increase in the cell volume was also moderately beneficial for Li^+ diffusion, as it reduced the polarization and internal resistance of the material during charging and discharging. Furthermore, because the binding energy of the Ti−O bond (662 kJ mol^{-1}) was higher than that of the Mn−O bond (402 kJ mol^{-1}),[40] Ti doping made the structure more stable.

The morphology and particle sizes of the samples were observed by scanning electron microscopy (SEM), as shown in Figure 3, and octahedron or polyhedron morphology is clearly visible. Furthermore, the samples contained smaller particles, resulting in larger contact areas between the particles and the electrolyte, a shorter Li^+ diffusion path, and a higher utilization rate of the active substances.[41,42] Doping of the Ti ions had little effect on the morphology and particle sizes of the obtained samples. However, it should be noted that the particle size distribution of the undoped $LiMn_2O_4$ was not uniform and the particles appeared to agglomerate, as shown in Figure 3a. Thus, doping of Ti likely improved the dispersion of the particles. Figure 3g shows the energy-dispersive spectrum of T3, where the presence of Ti element is clearly visible. This further confirmed the replacement of Ti ions into spinel $LiMn_2O_4$, as previously described.

2.2. Electrochemical Characterization. Figure 4 shows the initial discharge curves of $LiMn_{2-x}Ti_xO_4$, as well as the cycling performance curves at 0.2C at room temperature (RT). Figure 5a shows that two charging/discharging voltage platforms appeared at approximately 4.1 and 3.95 V on the charging/discharging curves, which corresponded to the two different stages of Li^+ insertion/extraction.[43,44] As shown in Figure 4a, the initial discharge capacities of samples T0, T1, T2, T3, T4, and T5 were 139.9, 129.5, 131.2, 136, 133.4, and 123 mAh g^{-1}, respectively. The discharge capacity of the undoped $LiMn_2O_4$ was the highest, and unlike the discharge capacities of the undoped sample, those of the doped Ti samples decreased to varying degrees. The T1 sample, which contained a small amount of Ti ions, exhibited a lower discharge capacity and may be due to the introduction of Ti ions into the material lattices. As a result, the Ti ions replaced part of the active Mn compounds, thus reducing the discharge capacity of the sample. However, when the Ti doping amount increased, the first discharge capacity initially increased and then decreased. As the Ti doping content increased, the particle structure of the sample became more regular, while the skeleton became more stable. This was conducive to the Li^+ insertion/extraction process. As a result, the electrochemical transformation between the trivalent manganese ions and tetravalent manganese ions could better adapt to the charge−discharge process. However, it should be noted that a relatively large Ti^{4+} doping amount resulted in a significant reduction in capacity. This likely occurred because the introduction of more Ti ions significantly reduced Mn ion content, producing numerous tiny agglomerated particles that could prevent the conduction and block the lithium-ion diffusion channel. Figure 4b shows the cycling performance of the samples at 0.2C, where the cycling performance of undoped $LiMn_2O_4$ was poor. After 300 cycles, the specific capacity of $LiMn_2O_4$ was only 52.5 mAh g^{-1}, with a capacity retention rate of 37.53%. Thus, the cycling performance of the doped Ti samples improved. After 300 cycles, the discharge-specific capacities of the T1, T2, T3, T4, and T5 samples were 62.4, 81.2, 106.2, 92.6, and 86.2 mAh g^{-1}, while the corresponding capacity retention rates were 48.19, 61.89, 78.09, 69.42, and 70.08%, respectively. In all of the doped samples, the T3 sample had the best capacity and cycling performance. Therefore, appropriate doping with Ti ions can effectively improve the electrochemical performance of the material.

Figure 5 shows the cycling performance curves of $LiMn_{2-x}Ti_xO_4$ (x = 0, 0.03) at 0.2C at 55 °C, whereby the capacity decay problem of $LiMn_2O_4$ was more serious at higher temperatures, as capacity was only 61.6 mAh g^{-1} after 100 cycles, while the capacity retention rate was 44.48%. However, the specific capacity of $LiMn_{1.97}Ti_{0.03}O_4$ was 102.3 mAh g^{-1} after 100 cycles at 55 °C, with a capacity retention rate of 75.44%, indicating that the Ti-doped materials performed better at higher temperatures.

Figure 6 shows the rate performance curves of $LiMn_{2-x}Ti_xO_4$ at different current densities from 0.2 to 10C at RT. This illustrates that the specific discharge capacities of the sample decreased as the current density increased. This occurred because the physical resistance and concentration polarization caused an overvoltage, which lowered the actual cutoff voltage during charging and discharging below the set value.[45] In particular, the rate performance of the undoped T0 sample was very poor under the large current density, with a discharge capacity of 31.3 mAh g^{-1} at 10C. However, the Ti-doped samples exhibited an enhanced rate performance, which was consistent with the results of the T1−T5 samples, as they had larger lattice constants and cell volumes. Of them, the T3 sample had the best rate performance, with specific capacities of 96.5 and 73.4 mAh g^{-1} at 5 and 10C, respectively. When the current density reverted to 0.2C, its specific capacity still reached 128 mAh g^{-1}, indicating that the T3 sample had good electrochemical reversibility. Moreover, the T3 sample retained good cycling performance under high current density. This indicated that Ti doping improved the high-rate discharge performance and utility of the active material.

To further investigate the effects of Ti doping on the structural stability of spinel $LiMn_2O_4$, the structures and morphologies of the T0 and T3 samples were characterized after 100 cycles at 0.5C at RT. Figure 7a shows the XRD patterns of the electrode samples, as well as pure $LiMn_2O_4$ before the electrochemical cycle, which was included for comparison. Except for the Al and C peaks, both the T0 and T3 sample diffraction peaks indicated spinel $LiMn_2O_4$, which were unchanged after 100 cycles. The peak intensity for T3 was stronger than that for T0, indicating that T3 had better crystallinity. The lattice parameters and cell volumes of the T0 and T3 samples after 100 cycles were calculated, and the results were compared with the parameters before the electrochemical cycle, as shown in Table 3. The internal stress caused by volume changes was not conducive to the structural stability of the material.[46] After 100 cycles, the volume shrinkage of the T3 sample was smaller, indicating that Ti doping enhanced the

https://doi.org/10.1021/acsomega.1c01521
ACS Omega 2021, 6, 21304−21315

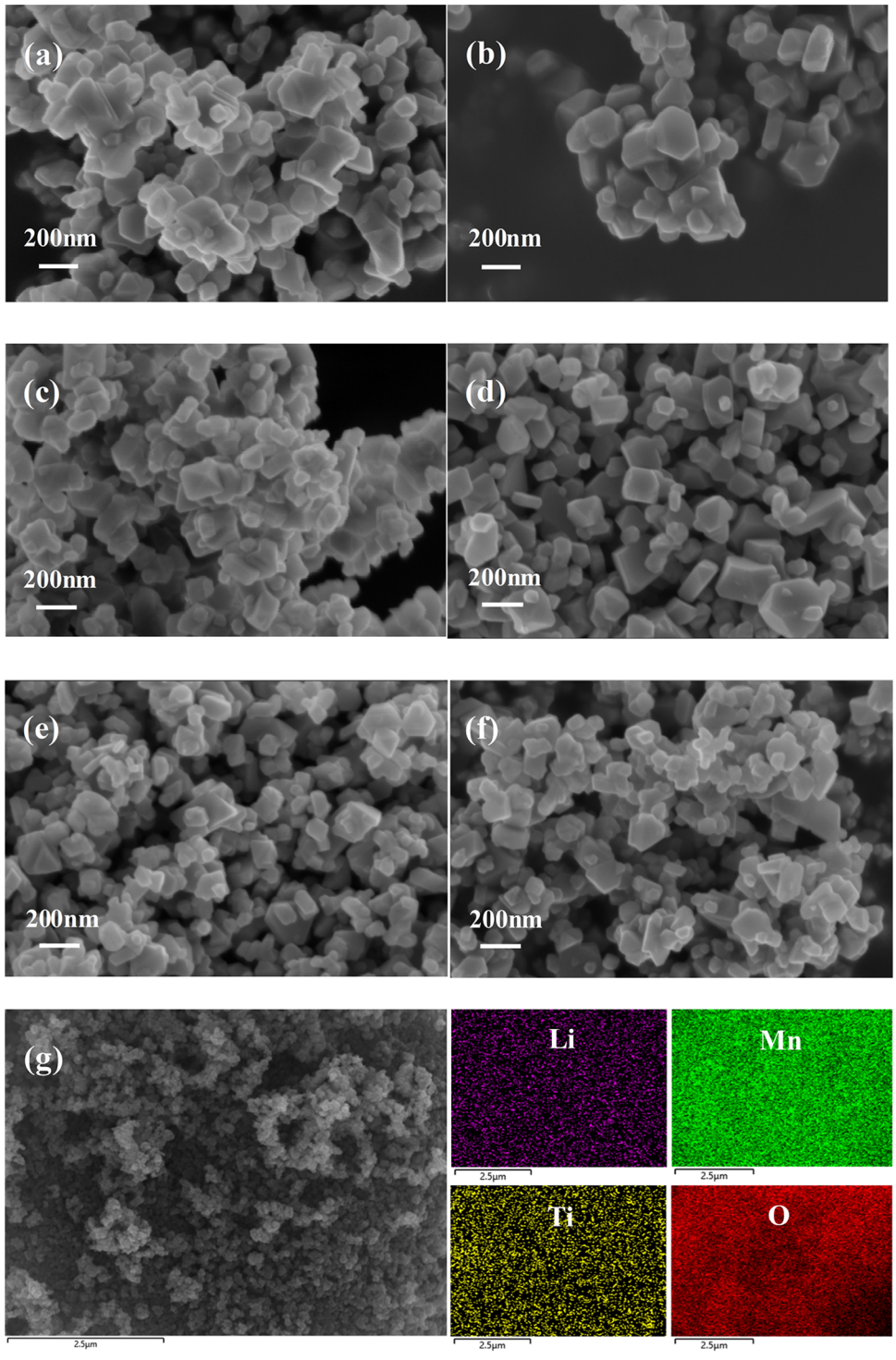

Figure 3. SEM images of the samples (a) T0, (b) T1, (c) T2, (d) T3, (e) T4, and (f) T5. (g) Energy-dispersive X-ray spectroscopy (EDS) mapping of T3.

structure of the material and alleviated the cycle capacity reduction issues. As shown in the T0 and T3 electrode SEM images, after 100 cycles at 0.5C (Figure 7b,c), the T0 surface contained more byproducts, while the T3 surface was relatively clean and intact. Therefore, doping with an appropriate amount of Ti appeared to be conducive to reducing the erosion of the electrolyte and maintaining the integrity of particles, thus improving the electrochemical performance of the material.

To further confirm the electrochemical behavior of the Ti-doped samples, cyclic voltammetry (CV) curves were recorded by scanning the T3 sample, which had the best electrochemical performance, along with the undoped T0 sample at 0.1−0.8 mV s^{-1}, as shown in Figure 8. The CV curves of $LiMn_2O_4$ and $LiMn_{1.97}Ti_{0.03}O_4$ were similar in shape, with both observing two pairs of redox peaks, indicating that Li-ion intercalation and deintercalation processes occurred in two steps,[47] which was consistent with the charging/discharging curves described

https://doi.org/10.1021/acsomega.1c01521
ACS Omega 2021, 6, 21304−21315

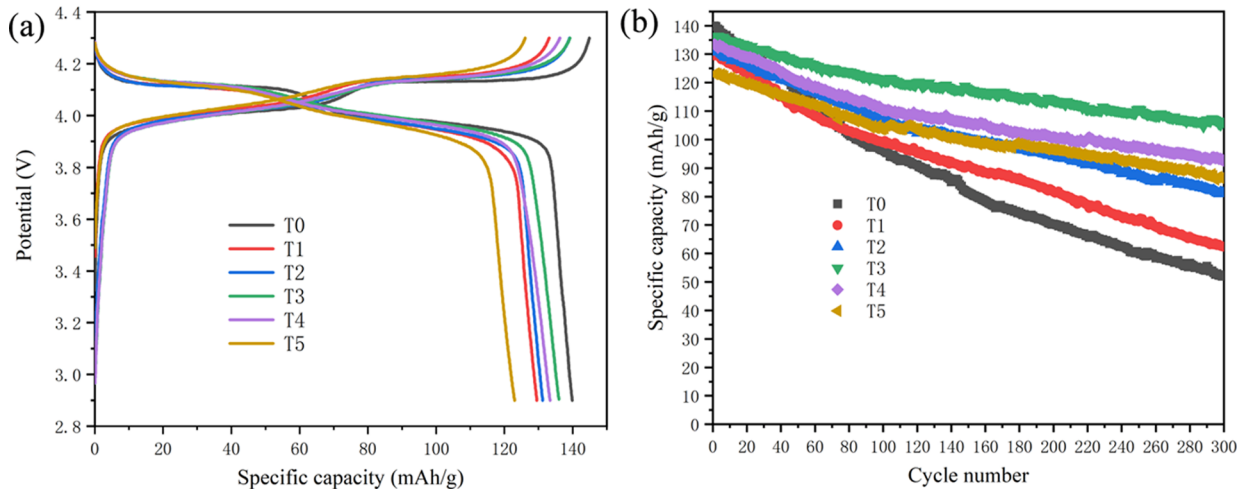

Figure 4. (a) Initial charge/discharge curves and (b) the cycling performance curves of the samples from T0 to T5 at 0.2C at RT.

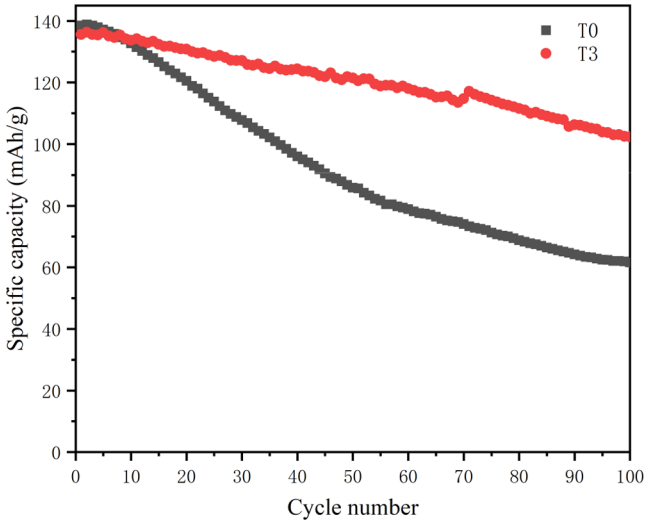

Figure 5. Cycling performance curves of T0 and T3 at 0.2C at 55 °C.

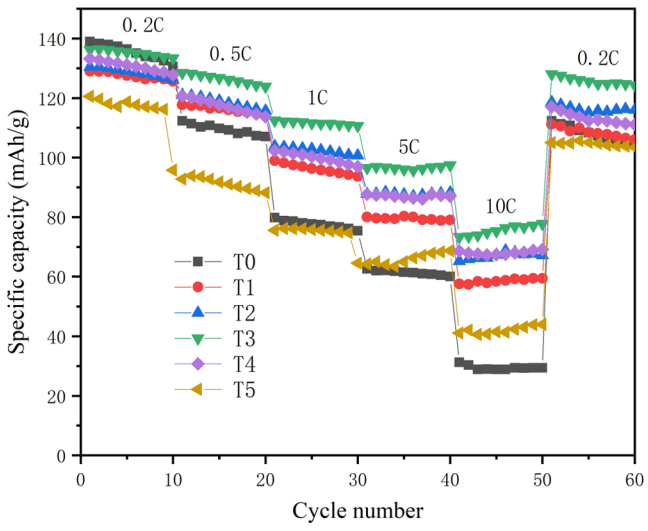

Figure 6. Rate capabilities of the samples from T0 to T5 at different current densities at RT.

above. As shown in Figure 8a,b, the peak potential of the samples moved to both sides as the scanning rate increased, reflecting the polarization reversibility. Figure 8c shows a good linear relationship between the square root of the scanning rate ($\nu^{1/2}$) and the peak current of the ipa2 peak (I_p), indicating that the charging and discharging processes of the lithium ions were diffusion-controlled processes. The diffusion coefficient of Li^+ (D_{Li^+}) can be calculated according to the following formula[48−51]

$$I_p = 2.69 \times 10^5 \times n^{3/2} \times A \times D_{Li^+}^{1/2} \times C_{Li^+} \times \nu^{1/2}$$

where I_p is the peak current (mA), n is the electron transfer number ($n = 1$), A is the electrode surface area (cm^2), C_{Li^+} is the concentration of Li^+ (0.02378 mol cm^{-3}), and ν is the scanning rate (mV s^{-1}). Therefore, the resulting D_{Li^+} values of T0 and T3 were 3.64×10^{-12} and 5.23×10^{-12} cm^2 s^{-1}, respectively. The T3 sample had a large Li-ion diffusion coefficient, indicating that the Li-ion diffusion rate was faster, which was consistent with the rate performance results.

To study the reaction kinetics of the Ti-doped $LiMn_2O_4$ cathode material in the cell, electrochemical impedance spectroscopy (EIS) measurements were performed on the T0 and T3 samples. Figure 9 shows the EIS spectra of the T0 and T3 samples after 1 and 100 cycles, respectively. The intercept between the semicircle and the x-coordinate in the high-frequency region represented the solution resistance of the electrolyte (R_s), while the semicircle of the intermediate frequency region was generated by the interaction of two resistors. These were denoted by solid electrolyte interface impedance (R_f) and charge-transfer impedance (R_{ct}), which are typically associated with the electronic conductivity of materials.[52] The increase in the semicircle indicated that the capacity for the partial charge transfer and the material transfer was reduced on the interface between the cathode and the electrolyte.[53] The sloped line represented the Warburg impedance (W_1), which was related to the rate of Li^+ diffusion in the electrode. As shown in Figure 9, the semicircle for the T0 sample was larger than that for the T3 sample, while the lithium-ion diffusion rate was faster in the T3 sample. Based on the principle of least square fitting, an equivalent circuit model was established to fit the experimental data, and the simulated impedance curves were in good agreement with the experimental data. Table 4 shows the fitted resistance values in the electrochemical impedance spectrum. After one cycle, the R_f and R_{ct} fitted values of T3 (36.22 and 46.19 Ω) were smaller than those of T0 (54.90 and 44.29 Ω). This showed that the T0

https://doi.org/10.1021/acsomega.1c01521
ACS Omega 2021, 6, 21304−21315

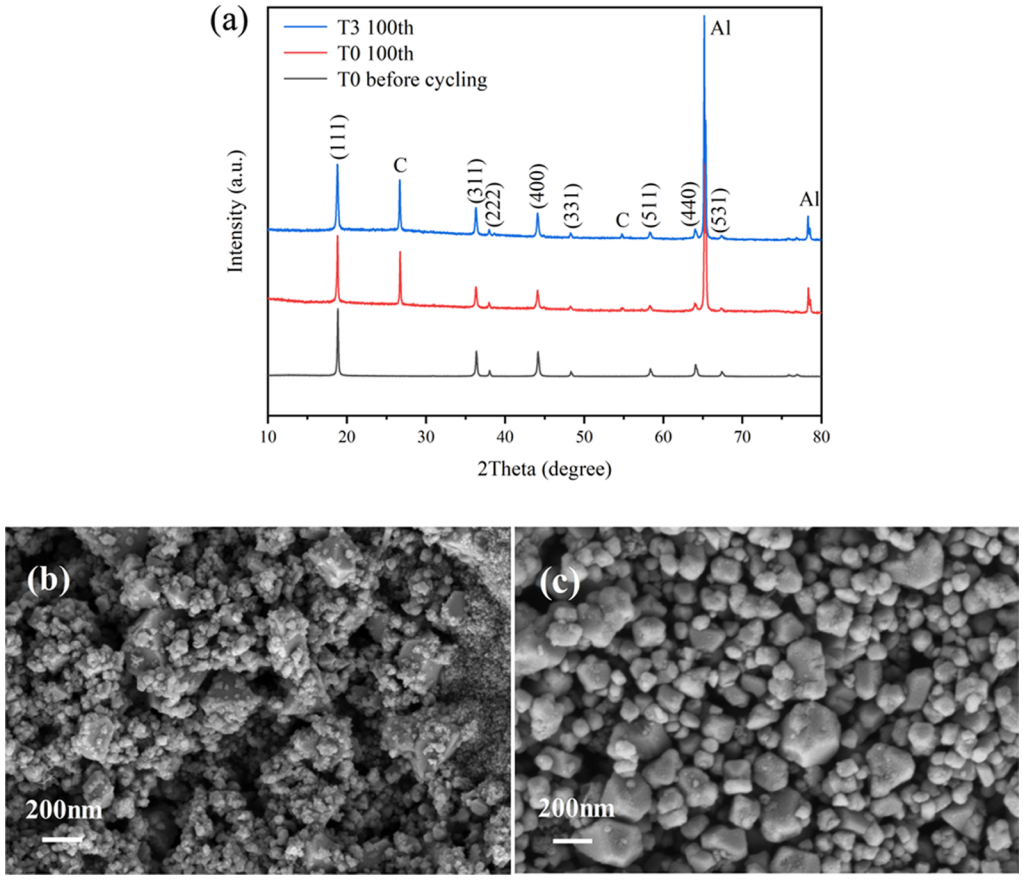

Figure 7. (a) XRD patterns of the T0 and T3 electrodes. (b, c) SEM images of the T0 and T3 electrodes after 100 cycles at 0.5C.

Table 3. Volume of T0 and T3 ($\triangle V$ Represents Their Volume Change before and after Cycling)

sample	V (Å^3) (before cycling)	V (Å^3) (100th)	ΔV (%)
T0	556.775	553.136	0.65
T3	558.107	556.874	0.22

sample had a large charge-transfer impedance and that doping with Ti improved the electron conductivity. After 100 cycles, the impedance difference between the T0 and T3 samples was more obvious, as the R_f and R_{ct} values for the T0 sample increased to 323.30 and 212.60 Ω and increased to 202.50 and 117.40 Ω for the T3 sample, respectively. The results indicated that after 100 cycles, the impedance inside the $LiMn_2O_4$ cathode material increased due to the distortion of the crystal structure. However, the Ti-doped $LiMn_2O_4$ material had a more stable crystal lattice, a more stable Li^+ diffusion channel, and lower charge-transfer resistance. Therefore, the T3 sample had better cycling performance and rate performance.

3. CONCLUSIONS

In this work, $LiMn_{2-x}Ti_xO_4$ was prepared using a one-step hydrothermal method. The structural characterization results showed that Ti was successfully doped into the samples, and Ti^{4+} replaced Mn^{4+} at the octahedral sites. All of the samples contained spinel structures, sharp diffraction peaks, and no impurity phases. The Ti doping has no significant effect on the morphology and size. Electrochemical tests showed that $LiMn_{1.97}Ti_{0.03}O_4$ exhibited better cycling performance and rate performance, where the first discharge-specific capacity was 136 mAh g^{-1} at 0.2C, and the discharge-specific capacity was 106.2 mAh g^{-1} after 300 cycles at 25 °C with a capacity retention of 78.09%. Additionally, the specific capacity of $LiMn_{1.97}Ti_{0.03}O_4$ was 102.3 mAh g^{-1} after 100 cycles at 55 °C, with a capacity retention rate of 75.44%. The structure and morphology of the samples after cycling also indicated that Ti doping enhanced the stability of the material's crystal structure, reducing the side reactions between the particle surface and the electrolyte. The CV and EIS spectra also showed that appropriate doping with Ti increases Li^+ diffusion while reducing the internal resistance of the electrode during charging and discharging. Therefore, our results indicated that the doping of Ti improved the electrochemical performance of spinel $LiMn_2O_4$.

4. EXPERIMENTAL SECTION

4.1. Synthesis of Materials. All samples were prepared using a hydrothermal method, where 0.21 g of $LiOH{\cdot}H_2O$ (AR, Aladdin), 0.79 g of $KMnO_4$, and TiO_2 (AR, Aladdin) were dissolved in 50 mL of deionized water, producing a 1:1 molar ratio of Li/Mn. Aniline was added to the mixture as a reducing agent and the solution was continuously stirred for 30 min. The aniline amount was calculated by controlling the molar ratio of aniline/$KMnO_4$, producing a 1:5 molar ratio of aniline/$KMnO_4$. Afterward, the resulting solution was moved into an autoclave, where it chemically reacted at 200 °C for 12 h, and the resulting mixture was filtered, dried, and ground to obtain $LiMn_{2-x}Ti_xO_4$ (x = 0, 0.01, 0.02, 0.03, 0.04, and 0.05) samples, which were denoted by T0, T1, T2, T3, T4, and T5, respectively.

4.2. Structural Characterization. X-ray photoelectron spectroscopy (XPS, Thermo Scientific K-Alpha) was used to

https://doi.org/10.1021/acsomega.1c01521
ACS Omega 2021, 6, 21304−21315

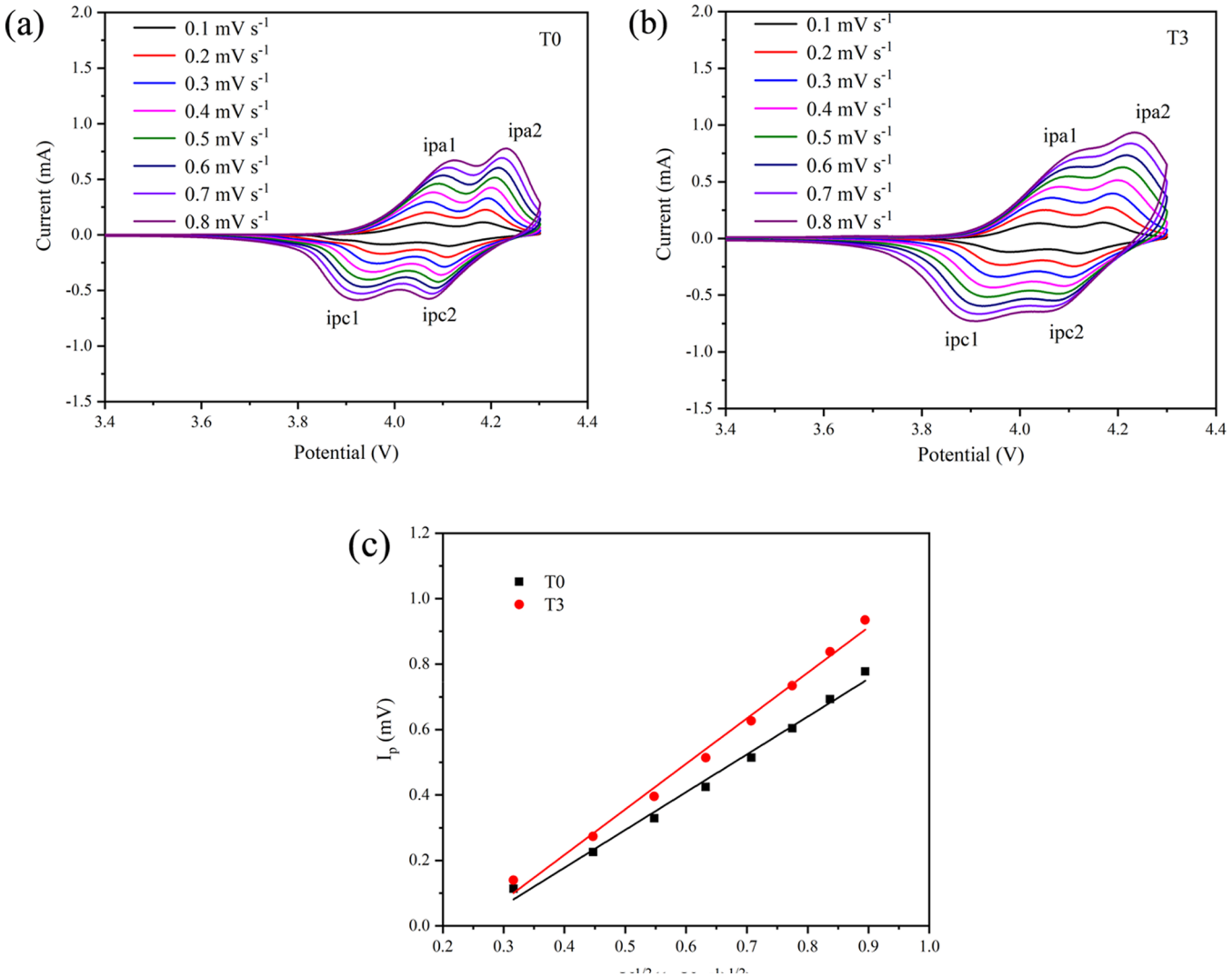

Figure 8. Cyclic voltammetry curves with various sweeping rates from 0.1 to 0.8 mV s^{-1}: (a) T0, (b) T3, and (c) peak current (I_p) of ipa2 as a function of the square root of the sweeping rate ($\nu^{1/2}$).

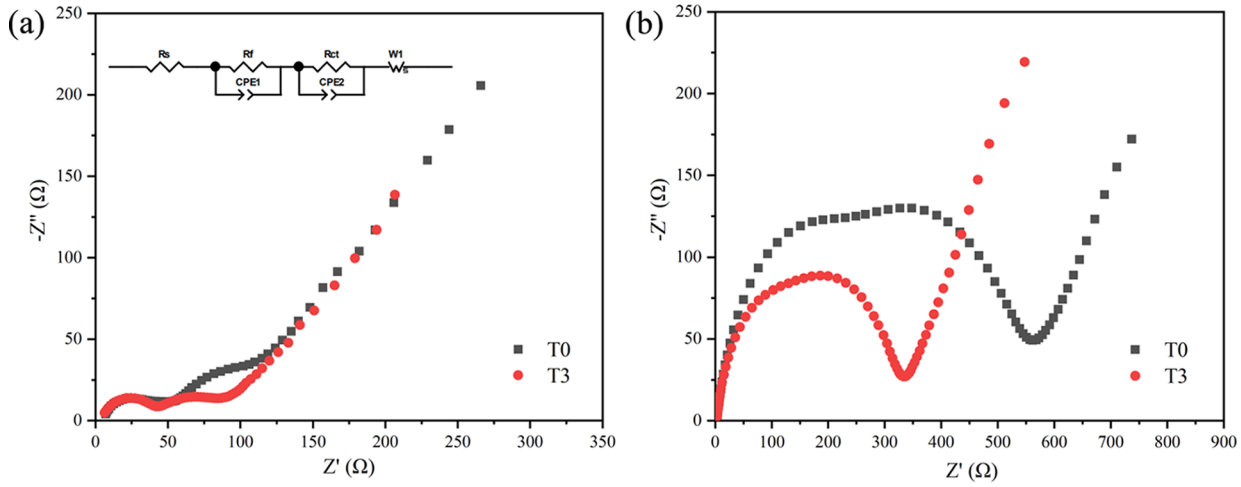

Figure 9. Electrochemical impedance spectroscopy plots for T0 and T3 (a) after 1 cycle and (b) after 100 cycles. Inset: the corresponding equivalent circuit diagram.

analyze the elemental surface composition and valence of the samples. The sample crystal structures were characterized via a X-ray diffractometer (XRD, Bruker D8 ADVANCE, Germany), where the radiation source was Cu Kα with a wavelength of 0.15406 nm, and diffraction peaks were obtained from 10 to 80°

https://doi.org/10.1021/acsomega.1c01521
ACS Omega 2021, 6, 21304−21315

Table 4. Fitted R_s, R_f, and R_{ct} Values as Obtained from Electrochemical Impedance Spectroscopy

	1st			100th		
sample	R_s (Ω)	R_f (Ω)	R_{ct} (Ω)	R_s (Ω)	R_f (Ω)	R_{ct} (Ω)
T0	4.63	54.90	44.29	2.72	323.30	212.60
T3	3.89	36.22	46.19	2.46	202.50	117.40

at 5° min^{-1}. The morphology was observed by scanning electron microscopy (SEM, Zeiss Sigma300, Germany).

4.3. Electrochemical Characterization. The obtained $LiMn_{2-x}Ti_xO_4$ samples, a poly(vinylidene fluoride) binder, and acetylene black were mixed together at a weight ratio of 8:1:1 and ground in an agate mortar, along with an *N*-methyl-2-pyrrolidone solvent to ensure uniform grinding. Afterward, the mixture was evenly coated on aluminum foil and dried in a vacuum drying oven at 110 °C to obtain the pole piece, and positive 11 mm diameter pole pieces were created via punching. The electrolyte solution consisted of $LiPF_6$ (1 M), with a volume ratio of 1:1:1 ethylene carbonate, 1,2-dimethyl carbonate, and ethyl methyl carbonate. The negative electrode was constructed from a lithium metal sheet, while porous polypropylene film (Celgard 2400) was used for the diaphragm. The cells were assembled into a button cell in an argon gas-filled glovebox. A battery test system (LAND-CT2001A, China) was then used to conduct a constant current charge−discharge experiment on the prepared semibattery. The charge−discharge cutoff potential was set between 2.9 and 4.3 V, while cyclic voltammetry and impedance were obtained using an electrochemical workstation (CHI600A, China).

AUTHOR INFORMATION

Corresponding Author

Hongyan Xie − *College of Material and Metallurgy, Guizhou University, Guiyang 550025, China; Guizhou Province Key Laboratory of Metallurgical Engineering and Process Energy Saving, Guiyang 550025, China; State Key Laboratory of Pressure Hydrometallurgical Technology of Associated Nonferrous Metal Resources, Kunming, Yunnan 650503, China*; Phone: 18285014076; Email: hyxie@gzu.edu.cn

Authors

Yaqing Zhang − *College of Material and Metallurgy, Guizhou University, Guiyang 550025, China; Guizhou Province Key Laboratory of Metallurgical Engineering and Process Energy Saving, Guiyang 550025, China*; orcid.org/0000-0002-5810-5644

Huixin Jin − *College of Material and Metallurgy, Guizhou University, Guiyang 550025, China; Guizhou Province Key Laboratory of Metallurgical Engineering and Process Energy Saving, Guiyang 550025, China*

Xiaohui Li − *College of Material and Metallurgy, Guizhou University, Guiyang 550025, China; Guizhou Province Key Laboratory of Metallurgical Engineering and Process Energy Saving, Guiyang 550025, China*

Qiang Zhang − *College of Material and Metallurgy, Guizhou University, Guiyang 550025, China; Guizhou Province Key Laboratory of Metallurgical Engineering and Process Energy Saving, Guiyang 550025, China*

Yezhu Li − *College of Material and Metallurgy, Guizhou University, Guiyang 550025, China; Guizhou Province Key Laboratory of Metallurgical Engineering and Process Energy Saving, Guiyang 550025, China*

KaiFeng Li − *College of Material and Metallurgy, Guizhou University, Guiyang 550025, China; Guizhou Province Key Laboratory of Metallurgical Engineering and Process Energy Saving, Guiyang 550025, China*

Fenglan Luo − *College of Material and Metallurgy, Guizhou University, Guiyang 550025, China; Guizhou Province Key Laboratory of Metallurgical Engineering and Process Energy Saving, Guiyang 550025, China*

Wenlei Li − *College of Material and Metallurgy, Guizhou University, Guiyang 550025, China; Guizhou Province Key Laboratory of Metallurgical Engineering and Process Energy Saving, Guiyang 550025, China*

Chenzhe Li − *College of Material and Metallurgy, Guizhou University, Guiyang 550025, China; Guizhou Province Key Laboratory of Metallurgical Engineering and Process Energy Saving, Guiyang 550025, China*

Complete contact information is available at: https://pubs.acs.org/10.1021/acsomega.1c01521

Notes

The authors declare no competing financial interest.

ACKNOWLEDGMENTS

This work was supported by the National Nature Science Foundation of China [grant no. 51764007].

REFERENCES

(1) Xia, H.; Luo, Z.; Xie, J. Nanostructured $LiMn_2O_4$ and their composites as highperformance cathodes for lithium-ion batteries. *Prog. Nat. Sci.: Mater. Int.* **2012**, *22*, 572−584.

(2) Winter, M.; Brodd, R. J. What are batteries, fuel cells, and supercapacitors? *Chem. Rev.* **2004**, *104*, 4245−4270.

(3) Bao, L.; Li, L.; Xu, G.; Wang, J.; Zhao, R.; Shen, G.; Han, G.; Zhou, S. Olivine $LiFePO_4$ nanocrystallites embedded in carbon-coating matrix for high power Li-ion batteries. *Electrochim. Acta* **2016**, *222*, 685−692.

(4) Yao, J.; Lv, L.; Shen, C.; Zhang, P.; Aguey-Zinsou, K.; Wang, L. Nano-sized spinel $LiMn_2O_4$ powder fabricated via modified dynamic hydrothermal synthesis. *Ceram. Int.* **2013**, *39*, 3359−3364.

(5) Wang, Y.; Zhu, B.; Wang, Y.; Wang, F. Solvothermal synthesis of $LiFePO_4$ nanorods as high-performance cathode materials for lithium ion batteries. *Ceram. Int.* **2016**, *42*, 10297−10303.

(6) Liu, Y.; Zhu, H.; Ren, Y.; Zhu, Y.; Huang, Y.; Dai, L.; Dou, S.; Xu, J.; Sun, C.; Wang, X.; Deng, Y.; Yuan, Q.; Liu, X.; Wu, J.; Chen, Y.; Liu, Q. Modulating the Surface Ligand Orientation for Stabilized Anionic Redox in Li-Rich Oxide Cathodes. *Adv. Energy Mater.* **2021**, *11*, No. 2003479.

(7) Lv, X.; Chen, S.; Chen, C.; Liu, L.; Liu, F.; Qiu, G. One-step hydrothermal synthesis of $LiMn_2O_4$ cathode materials for rechargeable lithium batteries. *Solid State Sci.* **2014**, *31*, 16−23.

(8) Kim, D. K.; Muralidharan, P.; Lee, H.; Ruffo, R.; Yang, Y.; Chan, C.; Peng, H.; Huggins, R.; Cui, Y. Spinel $LiMn_2O_4$ nanorods as lithium ion battery cathodes. *Nano Lett.* **2008**, *8*, 3948−3952.

(9) Xu, C.; Li, J.; Feng, X.; Zhao, J.; Tang, C.; Ji, B.; Hu, J.; Cao, C.; Zhu, Y.; Butt, F. K. The improved performance of spinel $LiMn_2O_4$ cathode with micro-nanostructured sphere-interconnected-tube morphology and surface orientation at extreme conditions for lithium-ion batteries. *Electrochim. Acta* **2020**, *358*, No. 136901.

(10) Liu, D.; Sun, S.; Yu, J. A new high-efficiency process for Li^+ recovery from solutions based on $LiMn_2O_4/\lambda$-MnO_2 materials. *Chem. Eng. J.* **2018**, *377*, No. 119825.

(11) Mao, F.; Guo, W.; Ma, J. Research progress on design strategies, synthesis and performance of $LiMn_2O_4$-based cathodes. *RSC Adv.* **2015**, *5*, 105248−105258.

(12) Huang, W.; Wang, G.; Luo, C.; Xu, Y.; Xu, Y.; Eckstein, B.; Chen, Y.; Wang, B.; Huang, J.; Kang, Y.; Wu, J.; Dravid, V.; Facchetti, A.;

Marks, T. Controllable growth of $LiMn_2O_4$ by carbohydrate-assisted combustion synthesis for high performance Li-ion batteries. *Nano Energy* **2019**, *64*, No. 103936.
(13) Guler, M. O.; Akbulut, A.; Cetinkaya, T.; Uysal, M.; Akbulut, H. Improvement of electrochemical and structural properties of $LiMn_2O_4$ spinel based electrode materials for Li-ion batteries. *Int. J. Hydrogen Energy* **2014**, *39*, 21447−21460.
(14) Xu, X.; Lee, S.; Jeong, S.; Kim, Y.; Cho, J. Recent progress on nanostructured 4V cathode materials for Li-ion batteries for mobile electronics. *Mater. Today* **2013**, *16*, 487−495.
(15) Darul, J.; Lathe, C.; Piszora, P. Hooked on switch: strain-managed cooperative Jahn-Teller effect in $Li_{0.95}Mn_{2.05}O_4$ spinel. *RSC Adv.* **2014**, *4*, 65205−65212.
(16) Wen, Y.; Ma, C.; Chen, H.; Zhang, H.; Li, M.; Zhao, P.; Qiu, J.; Ming, H.; Cao, G.; Tang, G. Stabilizing $LiMn_2O_4$ cathode in aqueous electrolyte with optimal concentration and components. *Electrochim. Acta* **2020**, *362*, No. 137079.
(17) Idemoto, Y.; Tejima, F.; Ishida, N.; Kitamura, N. Average, electronic, and local structures of $LiMn_{2-x}Al_xO_4$ in charge-discharge process by neutron and synchrotron X-ray. *J. Power Sources* **2019**, *410*−*411*, 38−44.
(18) Feng, X.; Tian, Y.; Zhang, J.; Yin, L. The effect of aluminum precursors on the structural and electrochemical properties of spinel $LiMn_{2-x}Al_xO_4$ (x = 0, 0.05, 0.1, 0.15) cathode materials. *Powder Technol.* **2014**, *253*, 35−40.
(19) Song, H.; Zhao, Y.; Niu, Y.; Wu, Z.; Hou, H. Applications of $LiCr_xMn_{2-x}O_4$ cathode material with high capacity and high rate in high-temperature battery. *Solid State Ionics* **2018**, *325*, 67−73.
(20) Xiang, M.; Ye, L.; Peng, C.; Zhong, L.; Bai, H.; Su, C.; Guo, J. Study on the electrochemical performance of high-cycle $LiMg_{0.08}Mn_{1.92}O_4$ cathode material prepared by a solid-state combustion synthesis. *Ceram. Int.* **2014**, *40*, 10839−10845.
(21) Luo, X.; Xiang, M.; Li, Y.; Guo, J.; Liu, X.; Bai, H.; Bai, W.; Su, C. Surface-orientation for boosting the high-rate and cyclability of spinel $LiNi_{0.02}Mn_{1.98}O_4$ cathode material. *Vacuum* **2020**, *179*, No. 109505.
(22) Wang, M.; Yang, M.; Zhao, X.; Ma, L.; Cao, G. Spinel $LiMn_{2-x}Si_xO_4$ (x < 1) through Si^{4+} substitution as a potential cathode material for lithium-ion batteries. *Sci. China Mater.* **2016**, *59*, 558−566.
(23) Son, J. T.; Kim, H. G. New investigation of fluorine-substituted spinel $LiMn_2O_{4-x}F_x$ by using sol-gel process. *J. Power Sources* **2005**, *147*, 220−226.
(24) Li, G.; Zhang, Z.; Huang, Z.; Yang, C.; Zuo, Z.; Zhou, H. Understanding the accumulated cycle capacity fade caused by the secondary particle fracture of $LiNi_{1-x-y}Co_xMn_yO_2$ cathode for lithium ion batteries. *J. Solid State Electrochem.* **2017**, *21*, 673−682.
(25) Venkateswara Rao, A.; Ranjith Kumar, B. Structural, electrical and electrochemical studies on doubly doped $LiMn_{2-x}(GdNi)_xO_4$ cathode materials for Li-ion batteries. *Mater. Lett.* **2018**, *227*, 250−253.
(26) Gao, R.; Sun, C.; Xu, L.; Zhou, T.; Zhuang, L.; Xie, H. Recycling $LiNi_{0.5}Co_{0.2}Mn_{0.3}O_2$ material from spent lithium-ion batteries by oxalate coprecipitation. *Vacuum* **2020**, *173*, No. 109181.
(27) Gu, H.; Wang, G.; Zhu, C.; Hu, Y.; Zhang, X.; Wen, W.; Yang, X.; Wang, B.; Gao, X.; Zhan, X.; Li, J.; Ma, Z.; He, Q. Correlating cycle performance improvement and structural alleviation in $LiMn_{2-x}M_xO_4$ spinel cathode materials: A systematic study on the effects of metal-ion doping. *Electrochim. Acta* **2019**, *298*, 806−817.
(28) Peng, C.; Huang, J.; Guo, Y.; Li, Q.; Bai, H.; He, Y.; Su, C.; Guo, J. Electrochemical performance of spinel $LiAl_xMn_{2-x}O_4$ prepared rapidly by glucose-assisted solid-state combustion synthesis. *Vacuum* **2015**, *120*, 121−126.
(29) Ram, P.; Gören, A.; Ferdov, S.; Silva, M.; Choudhary, G.; Singhal, R.; Costa, C. M.; Sharma, R. K.; Lanceros-Méndez, S. Synthesis and improved electrochemical performance of $LiMn_{2-x}Gd_xO_4$ based cathodes. *Solid State Ionics* **2017**, *300*, 18−25.
(30) Lu, J.; Zhan, C.; Wu, T.; Wen, J.; Lei, Y.; Kropf, A. J.; Wu, H. M.; Miller, D. J.; Elam, J. W.; Sun, Y.; Qiu, X.; Amine, K. Effectively suppressing dissolution of manganese from spinel lithium manganate via a nanoscale surface-doping approach. *Nat. Commun.* **2014**, *5*, No. 5693.
(31) Liu, J.; Li, G.; Bai, H.; Shao, M.; Su, C.; Guo, J.; Liu, X.; Bai, W. Enhanced cycle and rate performances of $Li(Li_{0.05}Al_{0.05}Mn_{1.90})O_4$ cathode material prepared via a solution combustion method for lithium-ion batteries. *Solid State Ionics* **2017**, *307*, 79−89.
(32) Guo, D.; Chang, Z.; Tang, H.; Li, B.; Xu, X.; Yuan, X.; Wang, H. Electrochemical performance of solid sphere spinel $LiMn_2O_4$ with high tap density synthesized by porous spherical Mn_3O_4. *Electrochim. Acta* **2014**, *123*, 254−259.
(33) Liu, H.; Tian, R.; Jiang, Y.; Tan, X.; Chen, J.; Zhang, L.; Guo, Y.; Wang, H.; Sun, L.; Chu, W. On the drastically improved performance of Fe-doped $LiMn_2O_4$ nanoparticles prepared by a facile solution-gelation route. *Electrochim. Acta* **2015**, *180*, 138−146.
(34) Jiang, Q.; Wang, X.; Zhang, H. One-pot hydrothermal synthesis of $LiMn_2O_4$ cathode material with excellent high-rate and cycling properties. *J. Electron. Mater.* **2016**, *45*, 4350−4356.
(35) Chen, K.; Donahoe, A.; Noh, Y. D.; Li, K.; Komarneni, S.; Xue, D. Conventional and microwave-hydrothermal synthesis of $LiMn_2O_4$: Effect of synthesis on electrochemical energy storage performances. *Ceram. Int.* **2014**, *40*, 3155−3163.
(36) Waller, G. H.; Lai, S. Y.; Rainwater, B. H.; Liu, M. Hydrothermal synthesis of $LiMn_2O_4$ onto carbon fiber paper current collector for binder free lithium-ion battery positive electrodes. *J. Power Sources* **2014**, *251*, 411−416.
(37) Tian, L.; Su, C.; Wang, Y.; Wen, B.; Bai, W.; Guo, J. Electrochemical properties of spinel $LiMn_2O_4$ cathode material prepared by a microwave-induced solution flameless combustion method. *Vacuum* **2019**, *164*, 153−157.
(38) Chen, S.; Chen, Z.; Cao, C. Mesoporous spinel $LiMn_2O_4$ cathode material by a soft-templating route. *Electrochim. Acta* **2016**, *199*, 51−58.
(39) Liu, Y.; Wang, J.; Wu, J.; Ding, Z.; Yao, P.; Zhang, S.; Chen, Y. 3D cube-maze-like Li-rich layered cathodes assembled from 2D porous nanosheets for enhanced cycle stability and rate capability of Lithium-Ion batteries. *Adv. Energy Mater.* **2019**, *10*, No. 1903139.
(40) Xiong, L.; Xu, Y.; Zhang, C.; Zhang, Z.; Li, J. Electrochemical properties of tetravalent Ti-doped spinel $LiMn_2O_4$. *J. Solid State Electrochem.* **2011**, *15*, 1263−1269.
(41) Zhao, H.; Liu, S.; Wang, Z.; Cai, Y.; Tan, M.; Liu, X. $LiSi_xMn_{2-x}O_4$ ($x \leq 0.10$) cathode materials with improved electrochemical properties prepared via a simple solid-state method for high-performance lithium-ion batteries. *Ceram. Int.* **2016**, *42*, 13442−13448.
(42) Zhang, H.; Xu, Y.; Liu, D.; Zhang, X.; Zhao, C. Structure and performance of dualdoped $LiMn_2O_4$ cathode materials prepared via microwave synthesis method. *Electrochim. Acta* **2014**, *125*, 225−231.
(43) Prabu, M.; Reddy, M. V.; Selvasekarapandian, S.; Subba Rao, G. V.; Chowdari, B. V. R. (Li, Al)-co-doped spinel, $Li(Li_{0.1}Al_{0.1}Mn_{1.8})O_4$ as high performance cathode for lithium ion batteries. *Electrochim. Acta* **2013**, *88*, 745−755.
(44) Wu, X.; Li, X.; Xiao, Z.; Liu, J.; Yan, W.; Ma, M. Synthesis and characterization of $LiMn_2O_4$ powders by the combustion-assisted sol-gel technique. *Mater. Chem. Phys.* **2004**, *84*, 182−186.
(45) Xu, Y.; Chen, G.; Fu, E.; Zhou, M.; Dunwell, M.; Fei, L.; Deng, S.; Andersen, P.; Wang, Y.; Jia, Q.; Luo, H. Nickel substituted $LiMn_2O_4$ cathode with durable high-rate capability for Li-ion batteries. *RSC Adv.* **2013**, *3*, 18441−18445.
(46) Cheng, X.; Liu, M.; Yin, J.; Ma, C.; Dai, Y.; Wang, D.; Mi, S.; Qiang, W.; Huang, B.; Chen, Y. Regulating Surface and Grain-Boundary Structures of Ni-Rich Layered Cathodes for Ultrahigh Cycle Stability. *Small* **2020**, *16*, No. 1906433.
(47) Cai, Y.; Huang, Y.; Wang, X.; Jia, D.; Pang, W.; Guo, Z.; Du, Y.; Tang, X. Facile synthesis of $LiMn_2O_4$ octahedral nanoparticles as cathode materials for high capacity lithium ion batteries with long cycle life. *J. Power Sources* **2015**, *278*, 574−581.
(48) Zhang, C.; Su, J.; Wang, T.; Yuan, K.; Chen, C.; Liu, S.; Huang, T.; Wu, J.; Lu, H.; Yu, A. Significant improvement on electrochemical performance of $LiMn_2O_4$ at elevated temperature by atomic layer deposition of TiO_2 nanocoating. *ACS Sustainable Chem. Eng.* **2018**, *6*, 7890−7901.
(49) Yu, Y.; Xiang, M.; Guo, J.; Su, C.; Liu, X.; Bai, H.; Bai, W.; Duan, K. Enhancing high-rate and elevated-temperature properties of Ni-Mg

co-doped $LiMn_2O_4$ cathodes for Li-ion batteries. *J. Colloid Interface Sci.* **2019**, *555*, 64−71.
(50) Lu, Y.; Luo, X.; Bai, H.; Guo, J.; Xiang, M.; Su, C.; Liu, X.; Bai, W.; Wang, R. Investigating the enhanced kinetics of $LiNi_{0.08}Mn_{1.92}O_4$ cathode material by regulating calcination temperature for long life lithium-ion battery. *Vacuum* **2018**, *158*, 223−230.
(51) Xie, Y.; Wu, F.; Dai, X.; Mai, Y.; Gu, Y.; Jin, H.; Li, J. Excellent electrochemical performance of $LiNi_{0.5}Co_{0.2}Mn_{0.3}O_2$ with good crystallinity and submicron primary dispersed particles. *Int. J. Energy Res.* **2021**, *45*, 6041−6053.
(52) Ran, Q.; Zhao, H.; Hu, Y.; Shen, Q.; Liu, W.; Liu, J.; Shu, X.; Zhang, M.; Liu, S.; Tan, M.; Li, H.; Liu, X. Enhanced electrochemical performance of dualconductive layers coated Ni-rich $LiNi_{0.6}Co_{0.2}Mn_{0.2}O_2$ cathode for Li-ion batteries at high cut-off voltage. *Electrochim. Acta* **2018**, *289*, 82−93.
(53) Snyders, C.; Ferg, E. Electrochemical Impedance Spectroscopy (EIS) study of doped spinel manganese cathode oxide materials synthesized for Li-ion batteries. *Mater. Today: Proc.* **2018**, *5*, 10450−10459.

https://doi.org/10.1021/acsomega.1c01521
ACS Omega 2021, 6, 21304−21315